

Doped VS₂ as a high-performance electrode material for rechargeable Mg-ion batteries

Yingfang Li,¹ Kunlun Wu,^{2,*} Haoran Luo,¹ Meng Li,¹ Lei Wang,¹ Kuan Sun,¹ and Yujie Zheng^{1,†,‡}

¹*National Innovation Center for Industry-Education Integration of Energy Storage Technology, MOE Key Laboratory of Low-grade Energy Utilization Technologies and Systems, CQU-NUS Renewable Energy Materials & Devices Joint Laboratory, School of Energy & Power Engineering, Chongqing University, Chongqing 400044, China*

²*Chongqing Key Laboratory of Intelligent Equipment Safety and Reliable Technology, Chongqing Ceprei Industrial Technology Institute Co., Ltd., Chongqing 400000, China*

(Received 19 July 2023; revised 17 December 2023; accepted 17 January 2024; published 20 February 2024)

Two-dimensional (2D) vanadium disulfide (VS₂) can serve as a universal host for reversible intercalation and deintercalation of alkali and alkaline earth metal ions. However, its practical application in rechargeable metal-ion batteries is limited by its low energy density (559 Wh g⁻¹). Herein, the effects of O doping and C, O codoping on the electrochemical performance of 2D VS₂ used as anode for magnesium-ion batteries (MIBs) are investigated by first-principles calculations. Values of both the energy density and specific capacity increase with increasing O-doping concentration, and those of VSO are 2.17 times and 1.16 times higher than those of VS₂, respectively. However, due to the strong bond between O and Mg, the diffusion barrier of Mg atoms on 2D VSO is relatively high (1.02 eV). Further introduction of C (VSO_{0.75}C_{0.25}) can reduce the diffusion barrier of Mg atoms (0.80 eV) to a level comparable to that of VS₂. Meanwhile, the values of energy density and specific capacity of VSO_{0.75}C_{0.25} are 1.53 times and 1.17 times those of VS₂. Our results suggest that O doping and C, O codoping of 2D VS₂ are effective strategies to improve the overall performance of MIBs and it should be possible to generalize such doping strategies to other rechargeable MIBs based on 2D transition metal dichalcogenides.

DOI: 10.1103/PhysRevApplied.21.024038

I. INTRODUCTION

The use of energy storage systems combined with renewable clean energy is an effective approach to achieving global carbon neutrality in the coming decades. Rechargeable ion batteries (RIBs), as an important energy storage technology for mobile electronic devices, electric vehicles, and large-scale energy storage systems, have attracted a lot of research interest. As we have witnessed, lithium-ion batteries (LIBs), as one of the most mature types of RIB, have been widely used. However, owing the scarcity of lithium in the Earth's crust and the potential safety hazards caused by dendrite precipitation, it is not suitable for future large-scale energy storage applications [1]. The magnesium-ion battery (MIB) is considered to be one of the most likely new-generation RIBs to replace the LIB due to the abundance of magnesium, low cost, high volumetric specific capacity, high safety, low dendrite deposition, and small ion radius [2]. However, the existing MIBs are still far from achieving the goal of superior

performance required by ever-growing energy consumption. It is hard to find electrode materials that can overcome the sluggish diffusion kinetics caused by the high charge polarization of Mg, while having high intercalation and deintercalation reversibility, high energy density, and good cycle stability [3–7].

In contrast to three-dimensional (3D) materials, two-dimensional (2D) materials, such as graphene and graphyne [8,9], transition metal carbonitrides [10,11], transition metal oxides [12,13], and transition metal dichalcogenides (TMDs) [14–18], have attracted a lot of attention recently due to their layered structure that can facilitate ion insertion and extraction [19], and their large specific surface area that can provide electrochemically active sites for ion storage [20–22]. Synthesis of 2D materials is currently possible in the laboratory [23]. It is promising to develop new 2D materials by borrowing existing technologies for developing 3D metal sulfides, producing 2D materials at affordable prices in the future, and using them as electrode materials for ion batteries [24]. As a typical TMD, VS₂ has been studied as a battery electrode material for decades, and past research has mainly focused on the 3D structure of metal sulfides to explore its application in the field of batteries [25,26]. Recently, 2D VS₂ has been used

*wukunlun@ceprei.com

†yujiezheng@outlook.com

‡zhengyujie@cqu.edu.cn

as a universal electrode material for rechargeable alkali metal ions (Li^+ , Na^+ , K^+) [27], Zn^{2+} [28], Mg^{2+} [29], and their hybrid batteries [30], and is a rising star [31,32]. Zhou *et al.* [27] prepared atomic-layer thick VS_2 as the electrode material for the storage of alkali-metal ions and it shows relatively high reversible specific capacities and great cycling stability. He *et al.* [28] designed and assembled aqueous Zn/VS_2 batteries with a high capacity of $190.3 \text{ mA h g}^{-1}$ and an energy density of 123 Wh kg^{-1} at a current density of 0.05 A g^{-1} . Compared with conventional 2D VS_2 , monolayer VS_2 has a higher ion storage capacity. However, the application of monolayer VS_2 in ion batteries is still a relatively new field with the potential of its application in ion battery electrode materials still to be further studied and explored. Xue *et al.* [29] and Xie *et al.* [33] have expanded the interlayer spacing up to 10 \AA , meaning that VS_2 is already or is close to being a monolayer, to enhance the storage of magnesium, sodium, and potassium. Moreover, Wang *et al.* [34] investigated the electrochemical performance of monolayer VS_2 for Li, K, Mg, and Al batteries by using first-principles calculations, and the predicted theoretical capacities of Li, Mg, K, and Al are 1397 , 1863 , 466 , and 78 mA h g^{-1} , respectively. Both Yang *et al.* [17] and Wang *et al.* [34] reported that monolayer VS_2 has superior electrochemical performance compared to bilayer and bulk VS_2 when used as electrodes. In contrast to 3D materials, the experimental capacities of Li- and K-ion batteries based on VS_2 nanosheets have exceeded 1050 and 400 mA h g^{-1} [27], which are very close to their theoretical capacity of monolayer VS_2 . Recently, monolayer VS_2 has been successfully prepared experimentally by CVD and solution phase methods [35]. By integrating current techniques for synthesizing monolayer VS_2 with the ongoing advancements in material synthesis methods, it is anticipated that the production of monolayer VS_2 will become more economically viable in the near future. Although the electrochemical performance of monolayer VS_2 as an electrode material for MIBs is suitable, its energy density (559 Wh g^{-1}) is still relatively small. Therefore, it is necessary to study how to further improve the theoretical capacity and capability density of monolayer VS_2 .

An important strategy for the design and functionalization of novel materials is elemental doping, which can essentially alter the properties of the material, including electronic (electrochemical) [36–38], optical [39,40], and magnetic [41,42] properties. Recently, investigations on the improvement of RIBs through the single-atom doping or multiheteroatom doping of electrode materials have been reported [43–45]. For instance, Zhang *et al.* [43] partially replaced Se with S in SnSe to enhance its electrochemical and thermoelectric performance, and obtained a series of dual functional $\text{SnSe}_{1-x}\text{S}_x$ ($x = 0, 0.1, 0.2, 0.3, 0.4$, and 0.5) electrode materials. Shi *et al.* [44] prepared $\text{MoS}_{0.74}\text{Se}_{1.26}/\text{N}$ -doped carbon anodes by introducing S

in MoSe_2 , and its performance was significantly better than MoS_2/NC and MoSe_2/NC in Na^+ batteries. Jian *et al.* [46] established a method for tuning the O-doping concentration in CVD-grown 2D MoS_2 . Shi *et al.* [47] prepared C-doped titanium nitride films (TiN/C) without a binder as electrodes for supercapacitors using the magnetron cosputtering technique. The TiN film electrode with approximately 5.33 at. % doped C exhibited remarkable capacitance performance, achieving a maximum areal capacitance of 45.81 mF cm^{-2} . These doping methods can serve as valuable references for doping with O and O, C in VS_2 . However, to our knowledge, elemental doping to improve the electrochemical performance of 2D VS_2 as an electrode has rarely been reported [48,49]. Tomar *et al.* [48] investigated the catalytic activity of pure and non-metallic (carbon, nitrogen, and phosphorus) functionalized 2D vanadium dichalcogenides (VS_2 , VSe_2 , and VTe_2). Of all the pristine monolayers, the pristine VS_2 monolayer is the most active HER (hydrogen evolution reaction) and OER (oxygen evolution reaction) catalyst, while for the functionalized case, the C-doped VS_2 monolayer has the best HER performance. Woo *et al.* [49] reported a method to obtain 2D transition metal dichloride matrices with better catalytic performance than that of carbon-based cathodes by F- and N-doping on H- VS_2 .

In this paper, in order to further improve the theoretical specific capacity and energy density of monolayer VS_2 for MIBs while maintaining its basic structure and good cycle stability, we investigated the electrochemical performance after partially replacing S with O, which has a smaller atomic weight. The electrochemical performance of a series of $\text{VS}_{2-x}\text{O}_x$ ($x = 0, 0.25, 0.5, 0.75$, and 1) was investigated by calculating the electronic structure, open-circuit voltage (OCV), theoretical capacity, energy density, and migration energy barrier of magnesium ions. We found that both specific capacity (up to 2165 mA h g^{-1}) and energy density (up to 1212 Wh g^{-1}) increased with increasing O-doping concentration. Unfortunately, the migration barrier (up to 1.02 eV) of Mg atoms also increased due to the strong bond between O and Mg. To reduce the migration barrier of Mg, we further introduced carbon (C), which has a similar atomic mass but lower electronegativity compared to O, into the 2D VSO system. We found that C and O codoping can increase the specific capacity (2187 vs 1863 mA h g^{-1}) and energy density (853 vs 559 Wh g^{-1}) of VS_2 while maintaining its average OCV (0.39 vs 0.30 V), conductivity, and low Mg atom migration barrier (0.803 vs 0.497 eV). Our results demonstrate that C, O codoping is a very effective strategy to improve the overall performance of 2D VS_2 -based MIBs, which will promote the widespread application of MIBs.

II. COMPUTATIONAL METHODS

All calculations based on first-principles calculations were performed in the framework of density-functional

theory (DFT), as implemented in the Vienna *ab initio* simulation package (VASP) [50,51]. The exchange-correlation energy was considered using the Perdew-Burke-Ernzerhof generalization within the framework of generalized gradient approximation. A plane-wave approach was employed with a cutoff energy set to 520 eV. Additionally, spin polarization and van der Waals correction (DFT-D3) [52] were taken into consideration in the calculations. A $2 \times 2 \times 1$ supercell with a vacuum separation larger than 20 Å was used to simulate the adsorption and diffusion of Mg cations on VS_xO_yC_z ($x + y + z = 2$) monolayers, and a $4 \times 4 \times 1$ K point was gridded in the Brillouin zone using the Monkhorst-Pack method. The conjugate gradient method was used for geometric optimization. The self-consistent calculations and electronic structure properties calculations were performed using a $7 \times 7 \times 1$ K grid. The climbing-image nudged elastic band method [53] was employed to calculate the Mg cation diffusion barriers on the VS_xO_yC_z monolayers with five or seven images. *Ab initio* molecular dynamics (AIMD) simulations were performed using VASP at a temperature of 300 K under an *NVT* system controlled by a Hoover thermostat [54]. The entire simulation time was 5 ps with a time step of 1 fs.

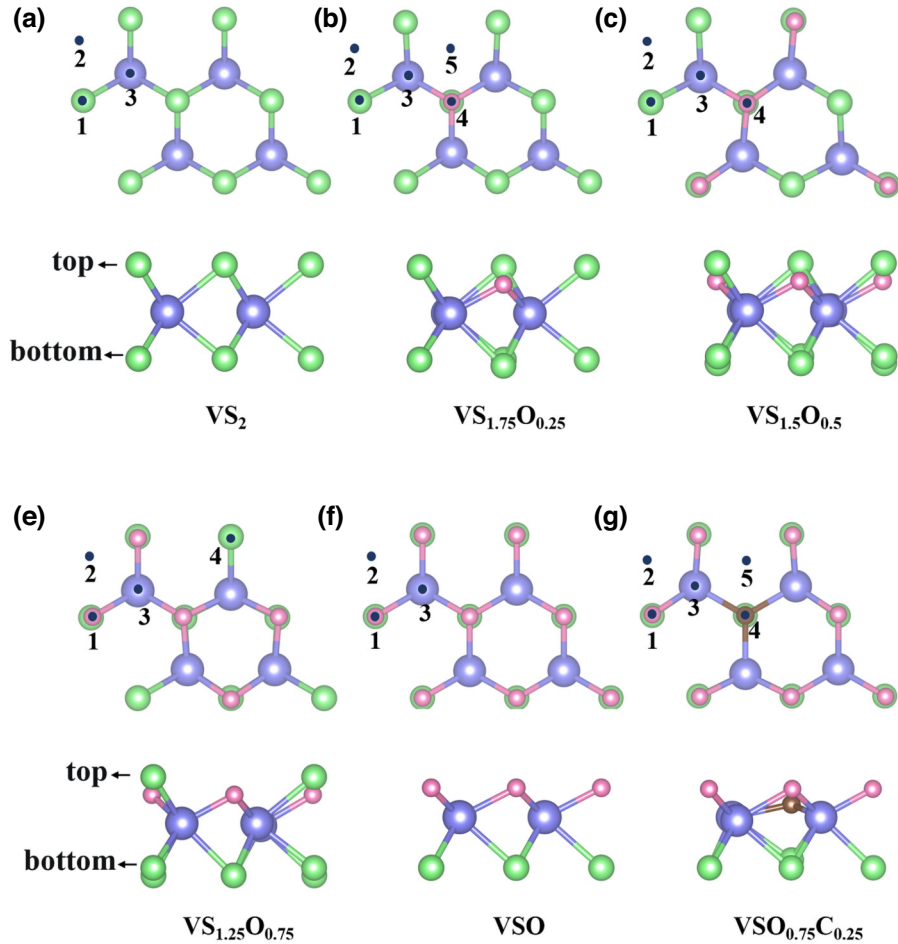


FIG. 1. Top and side views of the structure of VS_xO_yC_z, and possible adsorption sites of Mg atoms on the monolayer VS_xO_yC_z. (V, S, O, and C atoms are marked with purple, green, pink, and brown colors, respectively). The adsorption positions on the top and bottom surfaces are indicated by “top” and “bottom,” respectively. For example, 1-top, 2-top, and 3-top are the top sites on S, in the hollow, and on V of the top surface, respectively. (a), (b), (c), (d), (e), and (f) correspond to VS₂, VS_{1.75}O_{0.25}, VS_{1.5}O_{0.5}, VS_{1.25}O_{0.75}, VSO, and VSO_{0.75}C_{0.25}, respectively.

III. RESULTS AND DISCUSSION

A. Structure of VS_xO_yC_z monolayers

As shown in Fig. 1(a), pristine VS₂ has a graphene-like honeycomb lattice with a layer of S atoms at the top and bottom, and a layer of V atoms in the middle, forming a sandwich structure with a S-V-S spatial arrangement. Since there are two coordination numbers of the V atom with respect to the S atom, there are two phases of VS₂. In the *H* phase the V atom occupies the center of the trigonal prism formed by the S atoms, while in the *T* phase the V atom occupies the center of the octahedron formed by the S atoms. The *H* and the *T* phases are periodic 2D hexagonal lattices in both *x* and *y* directions. The *H*-phase VS₂ is more stable than the *T* phase, and monolayer *H*-phase VS₂ has been successfully prepared [55,56], so this paper focuses on the *H*-phase monolayer VS₂. It was important to find the most stable doping configuration, so we first tested several possible configurations for VS_{2-x}O_x ($x = 0.25, 0.5, 0.75$, and 1). According to the symmetry of VS₂, all the irreducible symmetry sites were selected for initial testing. In particular, as shown in Fig. S1 (in the Supplemental Material [57]), VS_{1.5}O_{0.5} and VS_{1.75}O_{0.25} have three and two possible configurations,

which we named $\text{VS}_{1.5}\text{O}_{0.5-\alpha}$, $\text{VS}_{1.5}\text{O}_{0.5-\beta}$, $\text{VS}_{1.5}\text{O}_{0.5-\gamma}$ and $\text{VS}_{1.75}\text{O}_{0.25-\alpha}$, $\text{VS}_{1.75}\text{O}_{0.25-\beta}$, respectively. We first calculated the formation energy of the $\text{VS}_{2-x}\text{O}_x$, which is defined as

$$E_f = (E_{\text{VS}_{2-x}\text{O}_x} - E_{\text{VS}_2} + n\mu_S - n\mu_O)/n. \quad (1)$$

$E_{\text{VS}_{2-x}\text{O}_x}$ and E_{VS_2} are the total energies of VS_2 after and before O doping, respectively. μ_S and μ_O are the chemical potentials of the O and S atom with reference to O_2 and S crystals respectively. n is the doping number of O. Formation energies of all $\text{VS}_{2-x}\text{O}_x$ are summarized in Table S1 and all have negative values. The formation energies of $\text{VS}_{1.5}\text{O}_{0.5-\alpha}$ and $\text{VS}_{1.5}\text{O}_{0.5-\beta}$, are very close (-1.21 and -1.18 eV), while $\text{VS}_{1.25}\text{O}_{0.75-\alpha}$ (-1.22 eV) is more stable than $\text{VS}_{1.25}\text{O}_{0.75-\beta}$ (-1.07 eV). Unfortunately, $\text{VS}_{1.5}\text{O}_{0.5-\beta}$ deforms greatly after adsorption of Mg atoms. Its α angle (i.e., the angle between the axis perpendicular to the VS_2 plane and the axis in VS_2 plane) decreases from 90° to 86.43° , which does not meet the requirements of long-term cycle stability for battery electrodes. Therefore, the most stable configurations of both $\text{VS}_{1.5}\text{O}_{0.5}$ and $\text{VS}_{1.25}\text{O}_{0.75}$ have O atoms substitute S on the same side, which should be the same for VSO.

The migration barrier of Mg on VSO is relatively high (as we will see in later results), and in order to reduce the migration barrier of Mg, we further introduce C doping. The formation energies for a C atom substituting an M ($M = \text{O}$ or S) atom were obtained through Eq. (2) and are summarized in Table S2.

$$E_f = (E_{\text{total}} - E_{\text{VSO}} + n\mu_C - n\mu_M)/n, \quad (2)$$

where E_{total} and E_{VSO} are the total energies of VSO before and after C doping, respectively. μ_C and μ_M are the chemical potentials of the C atom and M ($M = \text{O}$ or S) monomers, respectively. n is the doping number of C. The formation energies (Table S2) of C substituting S and O are -2.44 and -2.39 eV, respectively, indicating that C can substitute both O and S and is thermodynamically stable. The substitution of O by C significantly reduces the diffusion energy of Mg. In contrast, the substitution of S does not reduce the diffusion energy of Mg. Therefore, we only consider the case where C is substituted for O. When further increasing the C-doping concentration from 0.25 to 0.5, there are also two possible doping configurations, that is, $\text{VSO}_{0.5}\text{C}_{0.5-\alpha}$ and $\text{VSO}_{0.5}\text{C}_{0.5-\beta}$ [Figs. S1(f) and S1(g)]. The formation energies of $\text{VSO}_{0.5}\text{C}_{0.5-\alpha}$ and $\text{VSO}_{0.5}\text{C}_{0.5-\beta}$ are -2.01 and -1.92 eV, respectively, indicating that the $\text{VSO}_{0.5}\text{C}_{0.5-\alpha}$ configuration is more stable. We further checked their thermodynamic stability using AIMD simulations. As shown in Fig. S2, minor fluctuations caused by vibrations of the atoms have no effect on the changes in the stable phases of the doped $\text{VS}_x\text{O}_y\text{C}_z$. However, since the electronegativity of C is less than that O, the adsorption

energy of the Mg atom on $\text{VSO}_{0.5}\text{C}_{0.5-\alpha}$ is smaller than that on $\text{VSO}_{0.75}\text{C}_{0.25}$, which will result in a lower OCV for $\text{VSO}_{0.5}\text{C}_{0.5}$. Because a lower OCV is not conducive to increasing the energy density of the electrode, it makes no sense to continue to increase the doping concentration of C.

As depicted in Figs. 1(b)–1(f), the most stable structures of the doped monolayer $\text{VS}_x\text{O}_y\text{C}_z$ are similar to that of the pristine monolayer VS_2 ; the bond lengths, thicknesses of the $\text{VS}_x\text{O}_y\text{C}_z$ layers with and without Mg adsorption, and their variation are summarized Table S3 [57–59]. The pristine VS_2 has $a = b = 3.17$ Å and a layer thickness of 5.085 Å, consistent with the previous results [56,60]. Overall, the thickness of $\text{VS}_x\text{O}_y\text{C}_z$ gradually decreases as the O-doping concentration increases. When Mg is present, the variation in the thickness of the $\text{VS}_x\text{O}_y\text{C}_z$ layers is less than 5%, which is considered stable.

B. Mg adsorption on $\text{VS}_x\text{O}_y\text{C}_z$ monolayers

In order to find the most stable adsorption site for Mg atoms on the $\text{VS}_x\text{O}_y\text{C}_z$ monolayers, it is necessary to calculate the adsorption energy. The expression for the adsorption energy E_{ad} is given by

$$E_{\text{ad}} = E_{\text{VS}_x\text{O}_y\text{C}_z\text{Mg}_n} - E_{\text{VS}_x\text{O}_y\text{C}_z} - nE_{\text{Mg}}, \quad (3)$$

where $E_{\text{VS}_x\text{O}_y\text{C}_z}$ and $E_{\text{VS}_x\text{O}_y\text{C}_z\text{Mg}_n}$ are the total energies of $\text{VS}_x\text{O}_y\text{C}_z$ supercell before and after Mg-atom adsorption, respectively; E_{Mg} is the energy of each Mg atom [9] in the crystal of the hexagonal Bravais lattice; and n is the number of adsorbed Mg atoms, where $n = 1$. Here, we only discuss cases of adsorption on the surface, as the insertion of Mg atoms into monolayer VS_2 is difficult and will lead to the breaking of the V–M bonds, causing instability [34]. Figure 1 shows all possible initial adsorption sites that we tested. Three, ten, eight, eight, six, and ten initial adsorption sites were calculated for VS_2 , $\text{VS}_{1.75}\text{O}_{0.25}$, $\text{VS}_{1.5}\text{O}_{0.5}$, $\text{VS}_{1.25}\text{O}_{0.75}$, VSO, and $\text{VSO}_{0.75}\text{C}_{0.25}$, respectively. The adsorption energies of all sites of the six structures after structural optimization are summarized in Table S4. The most stable adsorption site of pristine VS_2 is the 3-top site [Fig. 2(a)], which is consistent with the previous results [17,34]. The most stable adsorption sites on the top surfaces of $\text{VS}_{1.75}\text{O}_{0.25}$ [Fig. 2(b)], $\text{VS}_{1.5}\text{O}_{0.5}$ [Fig. 2(c)], $\text{VS}_{1.25}\text{O}_{0.75}$ [Fig. 2(d)], VSO [Fig. 2(e)], and $\text{VSO}_{0.75}\text{C}_{0.25}$ [Fig. 2(f)] are all the central site (5-top) with adsorption energies of -1.40 , -1.77 , -1.71 , -2.19 , and -1.02 eV, respectively, implying an exothermic spontaneous process. The most stable adsorption sites on the bottom surfaces of $\text{VS}_{1.75}\text{O}_{0.25}$, $\text{VS}_{1.5}\text{O}_{0.5}$, $\text{VS}_{1.25}\text{O}_{0.75}$, VSO, and $\text{VSO}_{0.75}\text{C}_{0.25}$ are all the V top site 3-bottom with adsorption energies of -0.82 , -0.63 , -0.16 , -0.33 , and 0.30 eV, respectively (Fig. S3). The positive adsorption energy indicates that a single Mg atom is not readily adsorbed on the bottom surface of

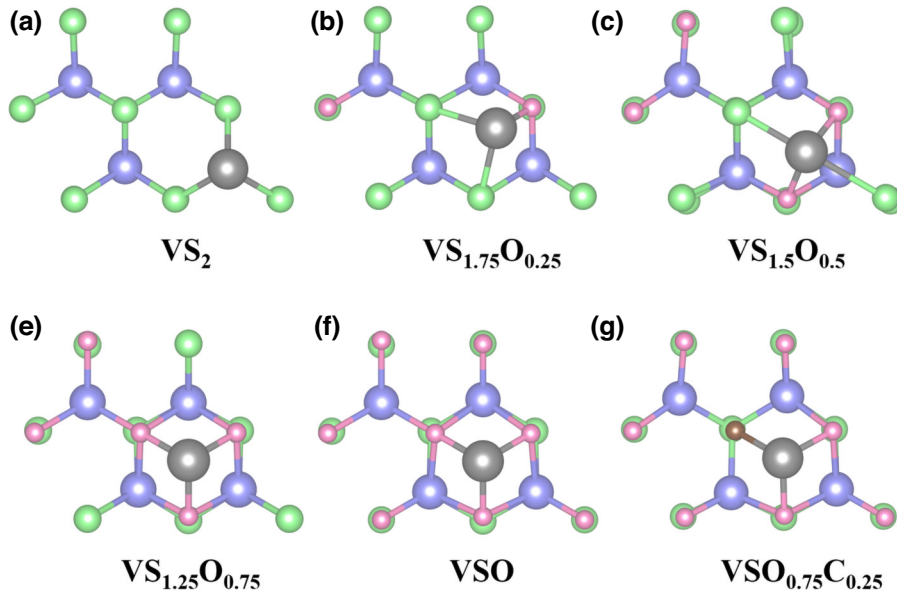


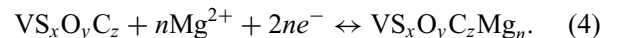
FIG. 2. The most stable adsorption sites on the top surfaces of VS₂ (a), VS_{1.75}O_{0.25} (b), VS_{1.5}O_{0.5} (c), VS_{1.25}O_{0.75} (d), VSO (e), and VSO_{0.75}C_{0.25} (f).

VSO_{0.75}C_{0.25}. This is because the electronegativity of C (3.15) is less than that of S (3.44) [61], i.e., the electron gaining ability of S > C. As will be shown below [in Fig. 8(d)], when C is introduced, the negatively charged region (green) around C on the top surface and the positively charged region (pink) in the middle shrinks, while the negatively charged region (green) around S on the bottom surface grows and a positively charged region (pink) on the bottom surface appears. Therefore, an electrostatic Coulomb repulsion is generated between this positively charged region and the Mg atoms, resulting in unstable adsorption of Mg atoms. However, when there is already a Mg atom adsorbed on the top surface at the same time, the C obtains electrons from both the Mg atom and the V atom on the top surface, and the positively charged region (pink) in the middle decreases, as shown in Figs. 9(f) and 9(g). In order to keep the system electrically neutral, the positively charged region (pink) around the bottom surface S disappears, and the electrostatic attraction with the Mg atom is restored, so the Mg atom adsorption on the bottom surface becomes stable again. As shown in Table S4, with the increase of O-doping concentration, the adsorption energy of Mg atoms increases; that is, the adsorption becomes more stable. When 0.25 of O in VSO is replaced by C, the adsorption energy of Mg decreases due to the electronegativity of C being less than that of O, resulting in a weaker binding between Mg and C atoms. However, the adsorption energy of Mg atoms on the surface of VSO_{0.75}C_{0.25} (-1.02 eV) is still greater than that of the pristine VS₂ (-0.87 eV); that is, the codoping of C and O is conducive to the adsorption of Mg atoms. Strong adsorption can effectively reduce the nucleation overpotential, but this in

turn results in higher diffusion energy. The higher desorption resistance and slower Mg migration rate due to strong adsorption severely reduce the multiplicity performance of the battery. In contrast, a weak adsorption is conducive to the diffusion of ions and accelerates the migration of Mg, but it also reduces the voltage as well as the adsorption stability of Mg, which is not conducive to the deposition of Mg. Therefore, the adsorption of Mg on the electrode surface should not be too strong or too weak. Interestingly, the adsorption energies of all VS_xO_yC_z monolayers are moderate, indicating a well-balanced relationship between diffusion and/or exfoliation.

C. Theoretical capacity and working potential

OCV and specific capacity are two key performance metrics for RIB electrodes. In order to investigate the effect of elemental doping on energy density, it is also necessary to explore the influence of the doping effect on OCV and specific capacity. Charging and discharging are mutually reversible reactions, and the half-reaction of a rechargeable battery is expressed as:



The OCV V of the electrode can be determined by the total energy difference before and after Mg atom adsorption. The Gibbs free energy at room temperature is approximately equal to the change in internal energy because both $P\Delta V$ and $T\Delta S$ are small and can be neglected [34], thus V is expressed as,

$$V = (E_{\text{VS}_x\text{O}_y\text{C}_z} + nE_{\text{Mg}} - E_{\text{VS}_x\text{O}_y\text{C}_z\text{Mg}_n})/2ne, \quad (5)$$

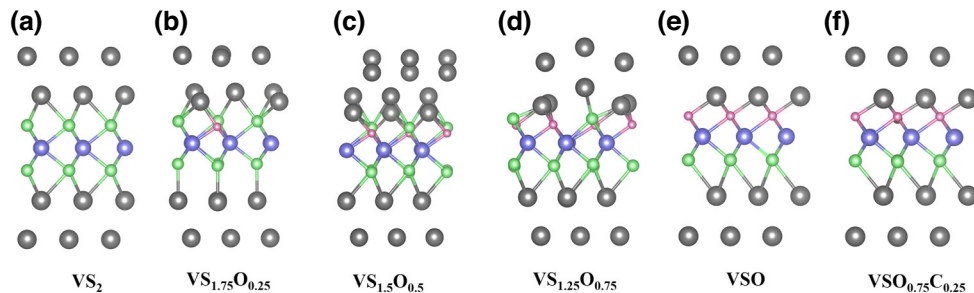


FIG. 3. Structure of the maximum adsorption of Mg atoms on $\text{VS}_x\text{O}_y\text{C}_z$: VS_2 (a), $\text{VS}_{1.75}\text{O}_{0.25}$ (b), $\text{VS}_{1.5}\text{O}_{0.5}$ (c), $\text{VS}_{1.25}\text{O}_{0.75}$ (d), VSO (e), and $\text{VSO}_{0.75}\text{C}_{0.25}$ (f).

where $E_{\text{VS}_x\text{O}_y\text{C}_z}$ and $E_{\text{VS}_x\text{O}_y\text{C}_z\text{Mg}_n}$ are the total energy before and after Mg atom adsorption, respectively; E_{Mg} is the energy of each Mg atom in the crystal of hexagonal Bravais lattice; n is the number of Mg atoms adsorbed; and 2 is the number of charges carried by Mg atoms.

To obtain the voltage profile we explored the maximum adsorption number of Mg atoms. The most stable adsorption site for the first layer of Mg on both the top and bottom surfaces of VS_2 is the 3-top site [Fig. 3(a)] with an adsorption energy of -0.394 eV per Mg atom, which is consistent with previously reported results [34]. The most stable adsorption sites for the first layer of Mg on the top and bottom surfaces of $\text{VS}_{1.75}\text{O}_{0.25}$ are the 2-top (5-top) and 1-bottom sites, respectively [Fig. 3(b)], and the adsorption energy is -0.438 eV per Mg atom. When a full layer is absorbed, we no longer strictly distinguish between 2-top and 5-top and denote them as 2-top (5-top). The most stable adsorption sites of the first layer of Mg on the top of $\text{VS}_{1.5}\text{O}_{0.5}$ [Fig. 3(c)], $\text{VS}_{1.25}\text{O}_{0.75}$ [Fig. 3(d)], VSO [Fig. 3(e)], and $\text{VSO}_{0.75}\text{C}_{0.25}$ [Fig. 3(f)] are all the 2-top (5-top) sites, while for the bottom surfaces of each of them are the 3-bottom, 3-bottom, 2-bottom (5-bottom), and 2-bottom (5-bottom) sites with adsorption energies of -0.495 , -0.481 , -0.566 , and -0.590 eV per Mg atom, respectively [Fig. S4(a)]. When the second Mg layers are adsorbed on the top and bottom surface, there are three possible adsorption sites, namely the 1-top, 2-top (5-top), and 3-top sites. The most stable adsorption sites for VS_2 , $\text{VS}_{1.75}\text{O}_{0.25}$, $\text{VS}_{1.5}\text{O}_{0.5}$, $\text{VS}_{1.25}\text{O}_{0.75}$, VSO , and $\text{VSO}_{0.75}\text{C}_{0.25}$ are all 1-top sites on the top surfaces, but the most stable adsorption sites on their bottom surfaces are 1-bottom, 3-bottom, 2-bottom (5-bottom), 2-bottom (5-bottom), 1-bottom, and 1-bottom, with adsorption energies -0.226 , -0.184 , -0.2 , -0.163 , -0.219 , and -0.263 eV per Mg atom, respectively [Fig. S4(b)]. Therefore, all four structures can adsorb up to four layers of Mg , which is consistent with the maximum adsorption of Mg on pristine VS_2 in a previous report [34].

Based on the adsorption energies of Mg atoms on $\text{VS}_x\text{O}_y\text{C}_z$ [Fig. 4(a)], OCV curves corresponding to the four structures were plotted according to Eq. (5)

[Fig. 4(b)]. Compared to the pristine VS_2 , the OCV curves of the doped $\text{VS}_x\text{O}_y\text{C}_z$ all moved upward, indicating that the OCV can be improved through O doping and C, O codoping. Specifically, the OCV increases with increasing O-doping concentration. When C partially replaces O, the OCV curve decreases significantly, but it is still higher than that of pristine VS_2 . This is the result of a decrease in adsorption energies caused by replacing the more electronegative O with the less electronegative C. The average voltages are shown in Fig. 4(c), and it can be seen that the average voltages of the doped $\text{VS}_x\text{O}_y\text{C}_z$ are higher than that of the pristine VS_2 . All of the calculated materials exhibit lower voltages, rendering them more suitable for use as anodes. Compared to magnesium, which is widely used as an anode in magnesium-ion batteries, the advantage of VS_2 lies in its ability to serve as a direct anode without the necessity of a protective layer. This inherent characteristic simplifies the battery design and manufacturing process, potentially leading to more efficient and cost-effective energy storage solutions.

The theoretical specific capacity is determined by the combination of the relative molecular mass of the host material, the maximum adsorption of the adsorbed ions, and the number of charges they carry when fully ionized, which is expressed as follows:

$$C = 2nF/M_{\text{VS}_x\text{O}_y\text{C}_z}, \quad (6)$$

where $M_{\text{VS}_x\text{O}_y\text{C}_z}$ is the relative molecular mass, F is the Faraday constant ($26\ 801$ mA h/mol), 2 is the valence of Mg atom at complete ionization, and n is the maximum adsorption amount of Mg atoms. Figure 4(d) summarizes the theoretical capacities of VS_2 , $\text{VS}_{1.75}\text{O}_{0.25}$, $\text{VS}_{1.5}\text{O}_{0.5}$, $\text{VS}_{1.25}\text{O}_{0.75}$, VSO , and $\text{VSO}_{0.75}\text{C}_{0.25}$ of 1863 , 1930 , 2003 , 2081 , 2165 , and 2187 mA h g $^{-1}$, respectively. The theoretical capacity of $\text{VS}_x\text{O}_y\text{C}_z$ increases with increasing O-doping concentration. Among them, $\text{VSO}_{0.75}\text{C}_{0.25}$ has the largest theoretical capacity, which is 17.39% higher than that of the pristine VS_2 . This is because lighter O and C atoms are used to substitute heavier S atoms, reducing

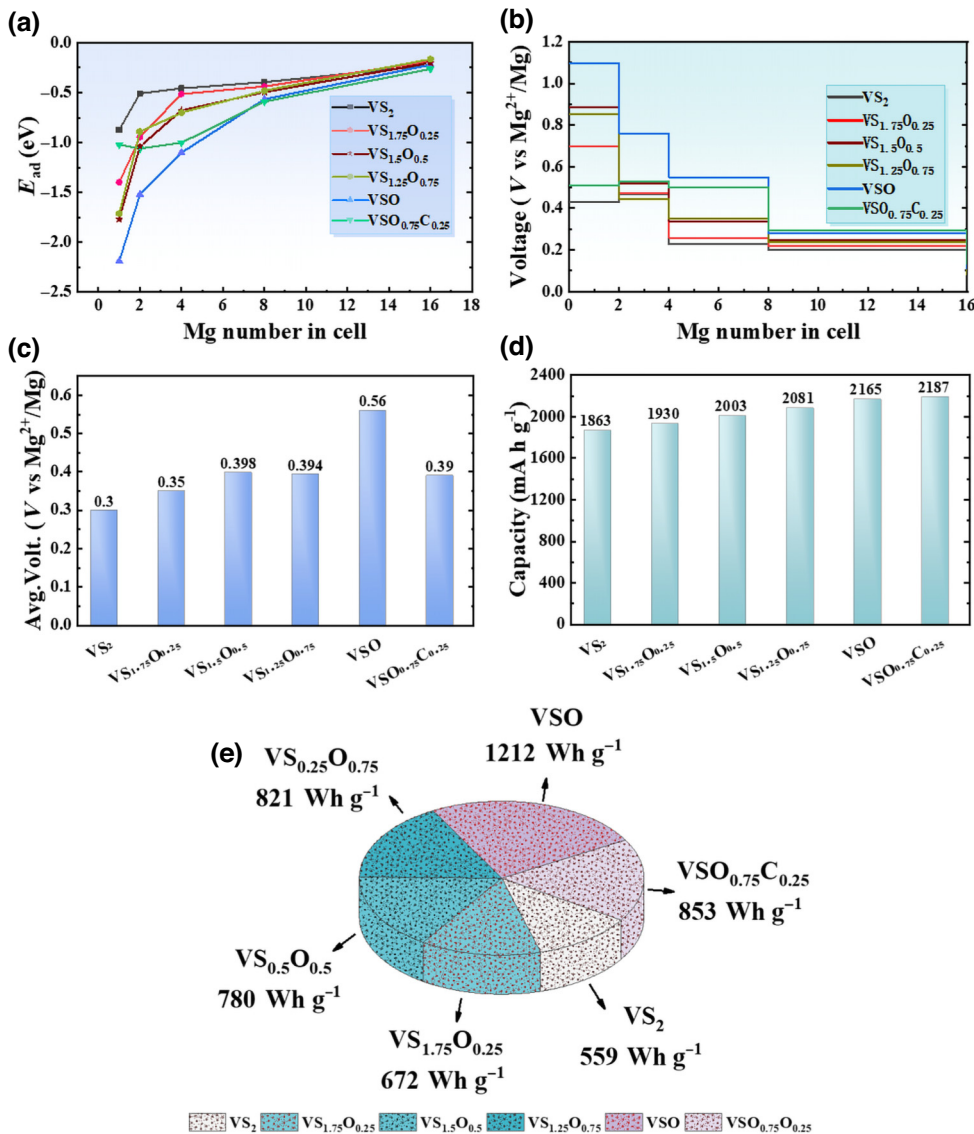


FIG. 4. (a) Adsorption energies of Mg on VS_xO_yC_z with the number of Mg atoms. (b) OCV curves of VS_xO_yC_z. (c) Average OCV of VS_xO_yC_z. (d) Theoretical specific capacity of VS_xO_yC_z. (e) The energy densities of VS_xO_yC_z.

the relative molecular mass of the host material, thereby increasing its theoretical capacity.

Energy density is determined by the OCV and the theoretical capacity, and is evaluated by the following formula:

$$E = CV, \quad (7)$$

where C is the theoretical capacity and V is the average OCV. The energy densities of VS₂, VS_{1.75}O_{0.25}, VS_{1.5}O_{0.5}, VS_{1.25}O_{0.75}, VSO, and VSO_{0.75}C_{0.25} were calculated to be 559, 672, 780, 821, 1212, and 853 Wh g⁻¹, respectively in Fig. 4(e). The energy densities of VS_xO_yC_z increase with increasing O-doping concentration. Compared with the pristine VS₂, the energy density of VSO is more than doubled. Unfortunately, the energy density of VSO_{0.75}C_{0.25}

after further introduction of C decreases compared to VSO, but is still 1.53 times higher than that of VS₂.

D. Mg atom diffusion kinetics on a VS_xO_yC_z monolayer

The diffusion barrier is one of the factors affecting the diffusion rate of metal ions, and it is also an important parameter determining the charge and/or discharge rate of RIBs. Figures 5 and S5 summarize all possible highly symmetric paths and their corresponding barriers for Mg migration on VS_xO_yC_z surfaces. All paths on the same surface are associated, i.e., they start at the same initial location and arrive at an agreed final state location. The top and bottom surfaces of VS₂ are symmetrical and only one surface needs to be considered. Taking the

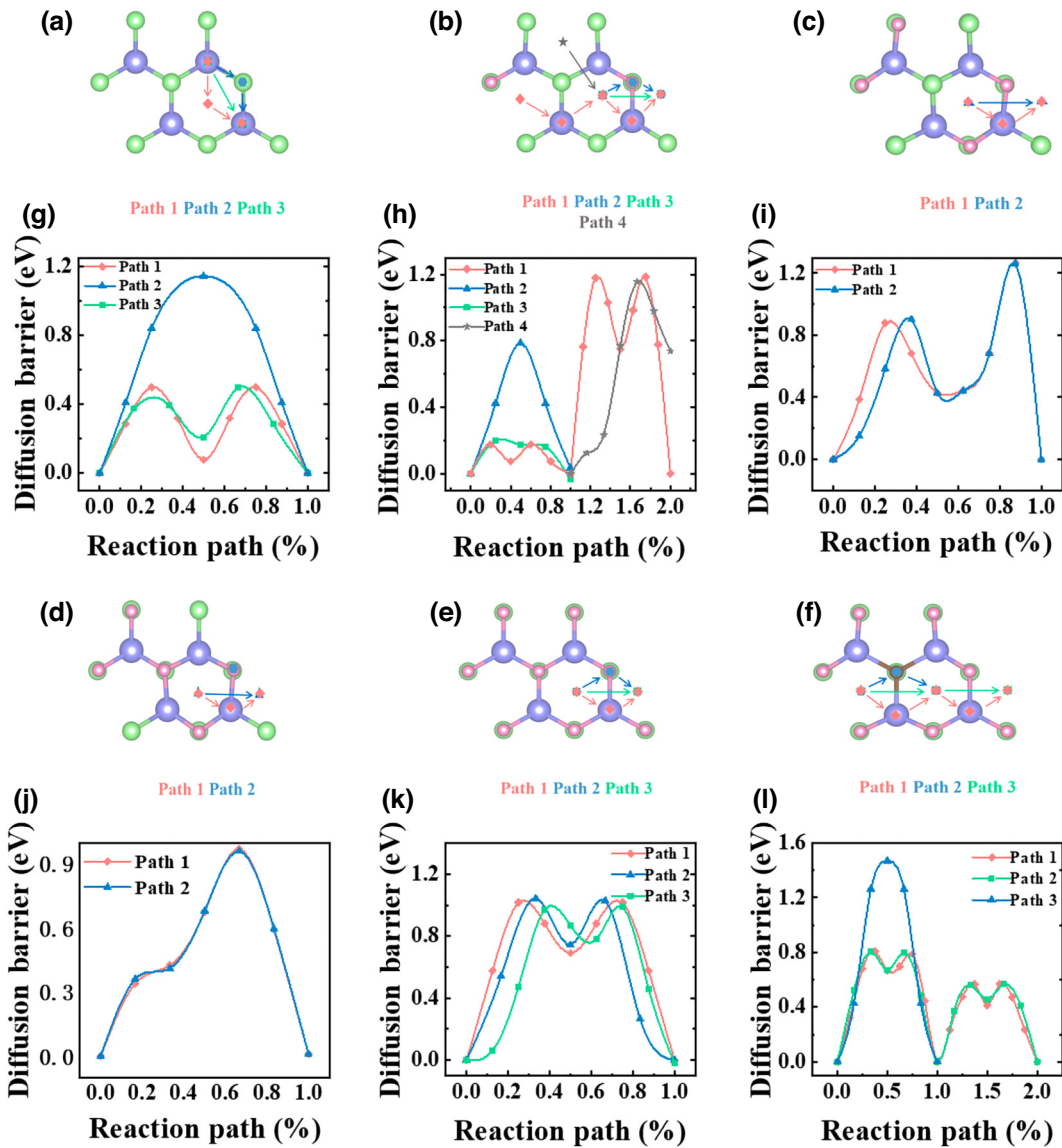


FIG. 5. The possible diffusion paths and their corresponding barriers on the top surface for VS₂ (a),(g), VS_{0.75}O_{0.25} (b),(h), VS_{1.5}O_{0.5}(c),(i), VS_{1.25}O_{0.75} (d),(j), VSO (e),(k), and VSO_{0.75}C_{0.25} (f),(l), respectively.

top surface as an instance, there are three diffusion paths [Fig. 5(a)] and their corresponding diffusion barriers are shown in Fig. 5(g). The lowest path is path 1 and its barrier is 0.497 eV, which is the same as the reported value [34]. The diffusions on the top and bottom surfaces of the doped VS_xO_yC_z need to be discussed separately due to their asymmetry. There are four, two, two, three, and three possible diffusion paths on the top surface of VS_{1.75}O_{0.25} [Figs. 5(b) and 5(h)], VS_{1.5}O_{0.5} [Figs. 5(c) and 5(i)], VS_{1.25}O_{0.75} [Figs. 5(d) and 5(j)], VSO [Figs. 5(e) and 5(k)], and VSO_{0.75}C_{0.25} [Figs. 5(f) and 5(l)], respectively. The lowest energy path for all of them is path 1, and the corresponding diffusion barriers are 1.185 (VS_{1.75}O_{0.25}), 1.260 (VS_{1.5}O_{0.5}), 0.970 (VS_{1.25}O_{0.75}), 1.016 (VSO), and 0.803 eV (VSO_{0.75}C_{0.25}). For the bottom surface,

VS_{1.75}O_{0.25} [Figs. S4(a) and S4(f)], VS_{1.5}O_{0.5} [Figs. S4(b) and S4(g)], VS_{1.25}O_{0.75} [Figs. S4(c) and S4(h)], VSO [Figs. S4(d) and S4(i)], and VSO_{0.75}C_{0.25} [Figs. S4(e) and S4(j)] all have two possible diffusion paths with minimum diffusion barriers of 0.515 (path 5), 1.26 (path 3), 0.97 (path 3), 0.292 (path 4), and 0.317 eV (path 4), respectively. The relatively large diffusion barrier on the VSO top surface is unfavorable to the migration of Mg cations. It has been reported that the surface exposed to C can effectively reduce the diffusion energy of Na ions on the surface of TiC₃ [62,63]. Moreover, the relative atomic mass of C is less than that of O, which is conducive to the theoretical capacity of MIBs; therefore, we further introduced C in VSO in an attempt to reduce the diffusion energy of the Mg cation. As we expected, when C was introduced to

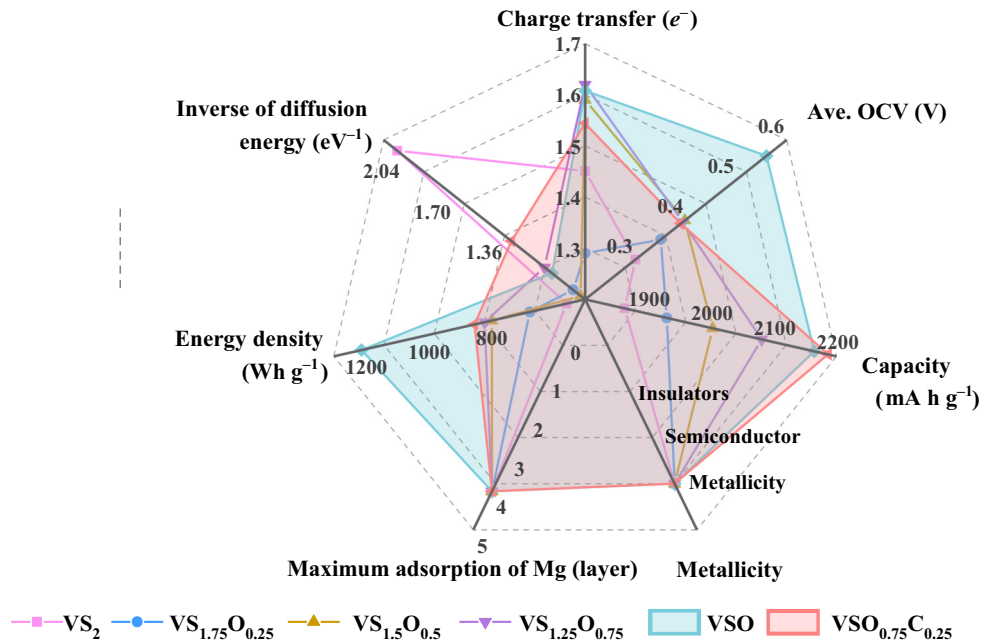


FIG. 6. The integrated performance diagram of $\text{VS}_x\text{O}_y\text{C}_z$. Clockwise from the top: charge transfer (e^-), the number of charges transferred at the most stable adsorption site; the average open circuit voltage; the theoretical capacity; the metallicity; the maximum adsorption of Mg atoms; the energy density; and the inverse of diffusion energy.

partially substitute O in VSO, the diffusion barrier on the top surface dropped from 1.016 to 0.803 eV with the barrier on the bottom surface remained consistent (0.292 vs 0.317 eV), demonstrating the kinetic of rapid Mg on the

surface of $\text{VSO}_{0.75}\text{C}_{0.25}$. Moreover, a comparison of the impact of C on ions' diffusion energy with other dopants is summarized in Fig. S6 in the Supplemental Material [57,64–71]. We can see that C is in the middle position.

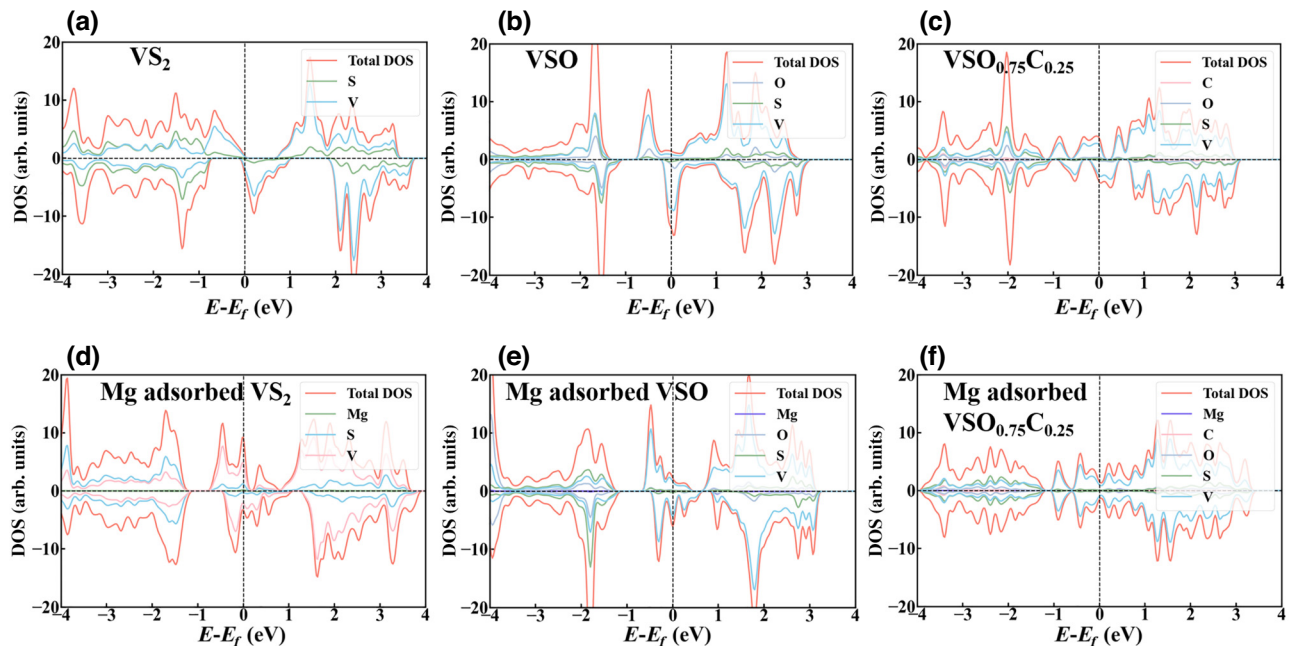


FIG. 7. (a),(b),(c) PDOS of VS_2 , VSO , and $\text{VSO}_{0.75}\text{C}_{0.25}$, respectively. (d),(e),(f) PDOS of VS_2 , VSO , and $\text{VSO}_{0.75}\text{C}_{0.25}$ after Mg is adsorbed on 5-top site, respectively.

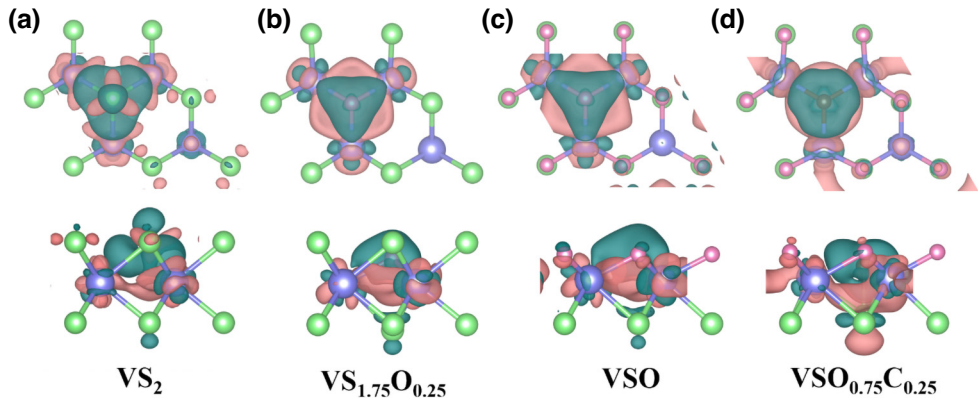


FIG. 8. (a),(b) The charge density difference isosurface for VS_2 before and after an O substitution of a S, respectively. (c),(d) The charge density difference for VSO before and after a C substitution of an O, respectively. Green and pink are electron-rich and electron-deficient regions, respectively. The isosurface level is set to $0.0025 \text{ e}/\text{\AA}^3$.

Although some elements have lower migration energy barriers than C, their atomic masses are much heavier, which is not conducive to increasing specific capacity.

A comprehensive comparison of these $\text{VS}_x\text{O}_y\text{C}_z$, including diffusion barrier (we inverted the diffusion energy in the radar diagram as the larger the overall area, the better performance), energy density, capacity, average OCV, and so on, are summarized in Fig. 6. Both OCV

and theoretical capacity increase with increasing O-doping concentration. Incorporation of diffusion energy suggests that increasing the O-doping concentration further is detrimental to the diffusion of Mg on the VS_2 surface, instead sacrificing the excellent multiplicative properties. Lower diffusion energy can be obtained by the introduction of C doping. Therefore, VSO (light blue area) has an intrinsically high energy density and OCV, and $\text{VSO}_{0.75}\text{C}_{0.25}$

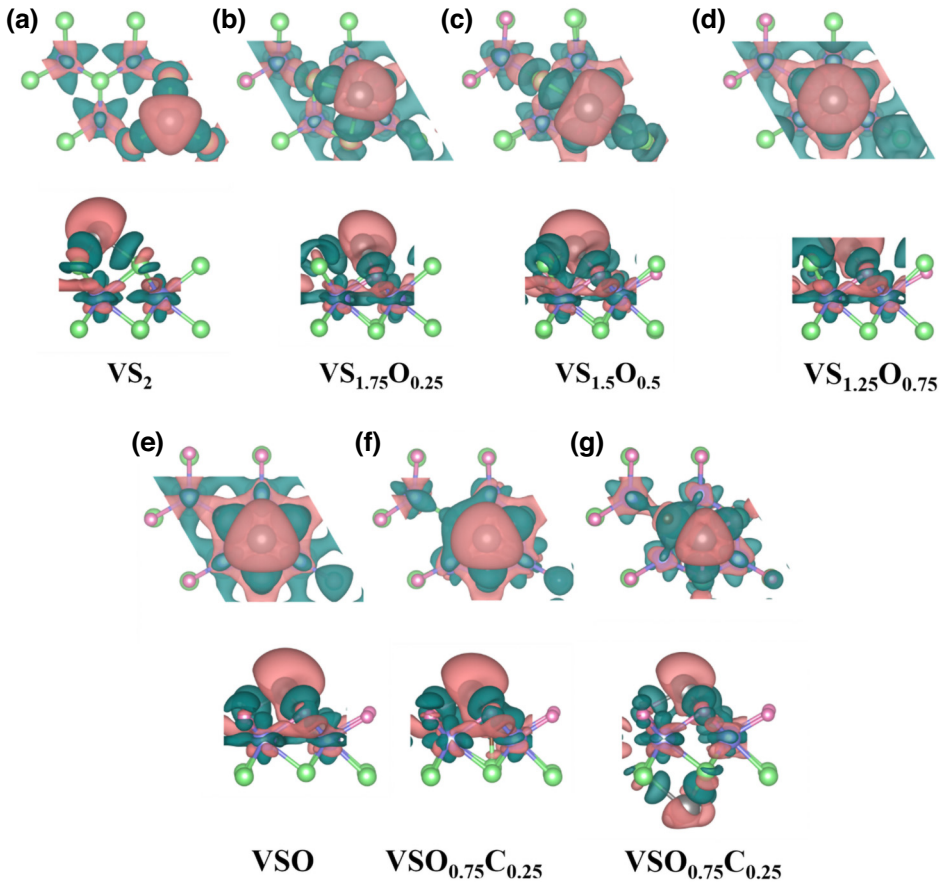


FIG. 9. Charge density isosurface configurations for Mg adsorbed on $\text{VS}_x\text{O}_y\text{C}_z$ monolayer: (a) on VS_2 , (b) on $\text{VS}_{1.75}\text{O}_{0.25}$, (c) on $\text{VS}_{1.5}\text{O}_{0.5}$, (d) on $\text{VS}_{1.25}\text{O}_{0.75}$, (e) on VSO, (f) on $\text{VSO}_{0.75}\text{C}_{0.25}$, and (g) on $\text{VSO}_{0.75}\text{C}_{0.25}$ both at the 5-top and 5-bottom sites. Green and pink are electron-rich and electron-deficient regions, respectively. The isosurface level is set to $0.0025 \text{ e}/\text{\AA}^3$.

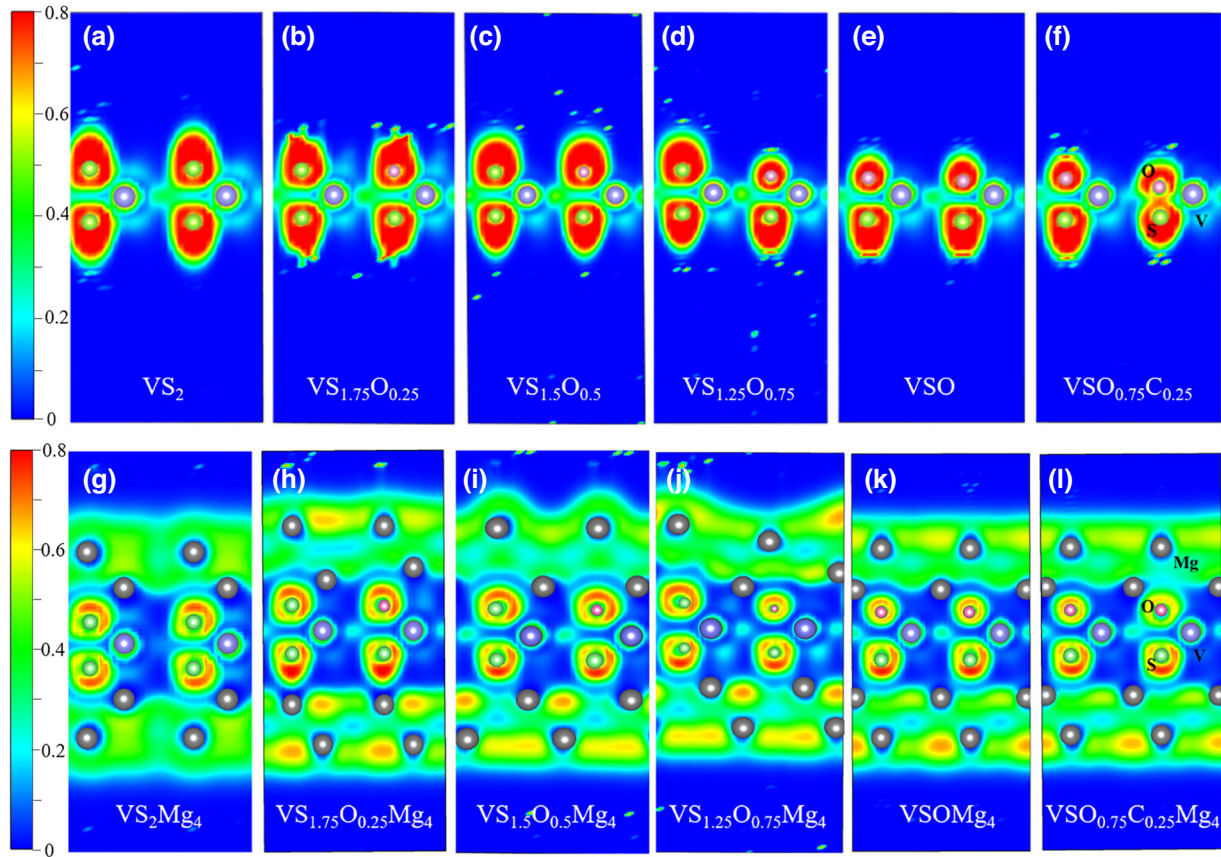


FIG. 10. Electron localization function isosurfaces (0.8) of the (110) slice of $\text{VS}_x\text{O}_y\text{C}_z$ monolayers without and with four Mg adsorption layers: (a),(g) VS_2 , (b),(h) $\text{VS}_{1.75}\text{O}_{0.25}$, (c),(i) $\text{VS}_{1.5}\text{O}_{0.5}$, (d),(j) $\text{VS}_{1.25}\text{O}_{0.75}$, (e),(k) VSO, and (f),(l) $\text{VSO}_{0.75}\text{O}_{0.25}$, respectively.

(light red area) performs better in terms of theoretical capacity and rate performance. Both of them have more significant electrochemical performance than VS_2 .

E. Electronic properties of $\text{VS}_x\text{O}_y\text{C}_z$ monolayers

To investigate the impact of elemental doping on the conductivity of VS_2 substrates and the effect after Mg atom adsorption on the electronic properties of $\text{VS}_x\text{O}_y\text{C}_z$, we calculated their projected density of states (PDOS) and projected band structures, and the results are shown in Figs. 7, S7, and S8. From the results, we can see that as the concentration of O doping increases, the d orbitals of V move towards lower energy compared with the Fermi level. When C is incorporated into VSO, the d orbitals of V move towards higher energies compared with the Fermi level. Compared with the pristine VS_2 , the DOS of the doped $\text{VS}_x\text{O}_y\text{C}_z$ increases at the Fermi level; that is, the doping improves the electronic conductivity of VS_2 . Interestingly, as the concentration of O doping increases the number of electrons occupying the Fermi energy level increases and all six structures exhibit metallicity, and the metallicity of these materials is not changed by the

adsorption of Mg atoms. These results indicate that all of them have excellent electronic properties.

Greater insight into the element doping and Mg atom adsorption process were obtained by evaluating the charge density difference $\Delta\rho$ using the following equation:

$$\Delta\rho = \rho_{AB} - \rho_A - \rho_B. \quad (8)$$

Here, A and B are the two fragments that make up AB . As showing in Figs. 8(a) and 8(b), when the S atom was replaced by the O atom, both the electron-rich region (green) and the electron-deficient region (pink) became larger. That is, the number of transferred charges increased because the electronegativity of O is larger than that of S, which enhances the adsorption of Mg atoms. In Figs. 8(c) and 8(d), when the O atom was replaced by the C atom, both the electron-rich region (green) and the electron-deficient region (pink) became smaller. Meanwhile the number of transferred charges decreased, which weakened the adsorption of Mg atoms since the electronegativity of C is less than O. This helps us understand the trend of the adsorption energy of Mg atoms on the $\text{VS}_x\text{O}_y\text{C}_z$ monolayers.

The adsorption process was further investigated by comparing the charge density isosurfaces of $\text{VS}_x\text{O}_y\text{C}_z$ before and after Mg atom adsorption. Figure 9 shows the charge density isosurface configurations for adsorbing Mg atoms at the most stable adsorption sites on the top surfaces of the $\text{VS}_x\text{O}_y\text{C}_z$ monolayers (other stable adsorption sites are included in Fig. S9). When electrons are transferred from Mg atoms to $\text{VS}_x\text{O}_y\text{C}_z$, there are electron-rich regions (pink) between $\text{VS}_x\text{O}_y\text{C}_z$ and Mg atoms, while there are obvious electron-deficient regions (green) around Mg atoms. The transfer of electrons proves that Mg atoms are bonded to $\text{VS}_x\text{O}_y\text{C}_z$ by ionic bonds. We further quantified the number of electrons transferred for the six structures at all stable adsorption sites by Bader charge analysis (see Table S5). The number of electrons transferred from the Mg atom to VS_2 (3-top) site is $1.451 e^-$. The number of electrons transferred from Mg atom to $\text{VS}_{1.75}\text{O}_{0.25}$, $\text{VS}_{1.5}\text{O}_{0.5}$, $\text{VS}_{1.25}\text{O}_{0.75}$, VSO, and $\text{VSO}_{0.75}\text{C}_{0.25}$ at the 5-top site is $1.56 e^-$, $1.60 e^-$, $1.30 e^-$, $1.61 e^-$, and $1.54 e^-$, respectively, and the numbers of electrons transferred at all other sites are less. Interestingly, the number of electrons transferred is more than 1 for all these structures, indicating that all of them are suitable as anodes for MIBs with double electron transfer of Mg during charge and discharge.

To further check the stability of the six structures before and after adsorption of four layers of Mg atoms, the electron localization function (ELF) calculations were performed, as shown in Fig. 10, based on a jelliumlike homogeneous electron gas and with ELF values renormalized in the range of 0 to 0.8. The ELF of the (110) section of the $\text{VS}_x\text{O}_y\text{C}_z$ monolayers without Mg adsorption reveal that the V— M ($M = \text{S}$, O, and C) bonds are ionic, indicating the presence of a high density of localized electrons between V and M . This suggests that the structure remains stable after doping. However, in the ELF analysis of $\text{VS}_x\text{O}_y\text{C}_z$ monolayers with four Mg layers, it is observed that the valence electrons of Mg atoms are sufficiently ionized to form a negative electron cloud within the cation layers. This electron cloud prevents repulsion between Mg atoms within the cation layers, consequently enhancing the adsorption stability. Meanwhile, the ionic character of the Mg— M ($M = \text{S}$, O, and C) bonds is also demonstrated by the presence of a high density of localized electrons between Mg and M , which also results in the stable adsorption of four layers of Mg.

IV. CONCLUSION

In this paper, the electrochemical performances of O-doped and C, O-codoped modified monolayer VS_2 as anodes for rechargeable MIBs were investigated using first-principles calculations. OCV, specific capacity, and energy density all increased with the increase of O-doping concentration. However, the diffusion barrier of Mg atoms also increased, leading to a decrease in

the rate performance of MIBs. To reduce the diffusion barrier of Mg atoms, C-doping was introduced on VSO. Compared to VSO, $\text{VSO}_{0.75}\text{C}_{0.25}$ has significantly improved conductivity and a low Mg atom diffusion barrier (0.80 vs 1.02 eV). The theoretical capacities of VSO and $\text{VSO}_{0.75}\text{C}_{0.25}$ are up to 2165 and 2187 mA h g⁻¹, respectively. Our results demonstrate that O doping and C, O codoping are very effective strategies to improve the overall performance of MIBs based on 2D VS_2 , which will promote the wide application of MIBs. Additionally, it should be possible to generalize the codoping strategy to other 2D TMDs. Combined with the multiatom codoping strategy, optimizing the type, proportion, and position of the dopants is expected to maximize the advantages of elemental doping.

ACKNOWLEDGMENTS

This work was financially supported by research grants from the Natural Science Foundation of China (Grant No. 12004057), Natural Science Foundation of Chongqing (Grant No. CSTB2022NSCQ-MSX1183), the support plan for Overseas Students to Return to China for Entrepreneurship and Innovation (Grant No. cx2020075), Open Fund of Key Laboratory of Low-grade Energy Utilization Technologies and Systems (Grant No. LLEUTS-2020008), and the numerical calculations in this paper have been done at the Hefei Advanced Computing Center.

The authors declare no conflicting interests.

- [1] B. Liu, J.-G. Zhang, and G. Shen, Pursuing two-dimensional nanomaterials for flexible lithium-ion batteries, *Nano Today* **11**, 82 (2016).
- [2] X. Liu, Y. Sun, Y. Tong, X. Wang, J. Zheng, Y. Wu, H. Li, L. Niu, and Y. Hou, Exploration in materials, electrolytes and performance towards metal ion (Li, Na, K, Zn and Mg)-based hybrid capacitors: A review, *Nano Energy* **86**, 106070 (2021).
- [3] X. Lei, X. Liang, R. Yang, F. Zhang, C. Wang, C. S. Lee, and Y. Tang, Rational design strategy of novel energy storage systems: Toward high-performance rechargeable magnesium batteries, *Small* **18**, 2200418 (2022).
- [4] X. Wu, Y. Dou, R. Lian, Y. Wang, and Y. Wei, Understanding rechargeable magnesium ion batteries via first-principles computations: A comprehensive review, *Energy Storage Mater.* **48**, 344 (2022).
- [5] J. Niu, Z. Zhang, and D. Aurbach, Alloy anode materials for rechargeable Mg ion batteries, *Adv. Energy Mater.* **10**, 2000697 (2020).
- [6] F. Liu, T. Wang, X. Liu, and L. Z. Fan, Challenges and recent progress on key materials for rechargeable magnesium batteries, *Adv. Energy Mater.* **11**, 2000787 (2020).
- [7] M. Guo, C. Yuan, T. Zhang, and X. Yu, Solid-state electrolytes for rechargeable magnesium-ion batteries: From structure to mechanism, *Small* **18**, 2106981 (2022).

- [8] Y. Zhang, X. Xia, B. Liu, S. Deng, D. Xie, Q. Liu, Y. Wang, J. Wu, X. Wang, and J. Tu, Multiscale graphene-based materials for applications in sodium ion batteries, *Adv. Energy Mater.* **9**, 1803342 (2019).
- [9] Y. Mao and H. Soleymanabadi, Graphyne as an anode material for Mg-ion batteries: A computational study, *J. Mol. Liq.* **308**, 113009 (2020).
- [10] Z. Xiaojun, W. Peng, L. Erfei, W. Chongchong, M. Kai, G. Zhengyang, D. G. Ian, and Y. Weijie, Screening MXenes for novel anode material of lithium-ion batteries with high capacity and stability: A DFT calculation, *Appl. Surf. Sci.* **569**, 151050 (2021).
- [11] H. Shi-Ping, Z. Jing, R. Yu-Rong, and C. Wen-Kai, Investigating the potentials of TiVC MXenes as anode materials for Li-ion batteries by DFT calculations, *Appl. Surf. Sci.* **569**, 151002 (2021).
- [12] M. Zheng, H. Tang, L. Li, Q. Hu, L. Zhang, H. Xue, and H. Pang, Hierarchically nanostructured transition metal oxides for lithium-ion batteries, *Adv. Sci.* **5**, 1700592 (2018).
- [13] Z. Liu, H. Su, Y. Yang, T. Wu, S. Sun, and H. Yu, Advances and perspectives on transitional metal layered oxides for potassium-ion battery, *Energy Storage Mater.* **34**, 211 (2021).
- [14] H. Su, S. Jaffer, and H. Yu, Transition metal oxides for sodium-ion batteries, *Energy Storage Mater.* **5**, 116 (2016).
- [15] P. Geng, S. Zheng, H. Tang, R. Zhu, L. Zhang, S. Cao, H. Xue, and H. Pang, Transition metal sulfides based on graphene for electrochemical energy storage, *Adv. Energy Mater.* **8**, 1703259 (2018).
- [16] X. Wang, Q. Weng, Y. Yang, Y. Bando, and D. Golberg, Hybrid two-dimensional materials in rechargeable battery applications and their microscopic mechanisms, *Chem. Soc. Rev.* **45**, 4042 (2016).
- [17] J. Yang, J. Wang, X. Dong, L. Zhu, D. How, W. Zeng, and J. Wang, The potential application of VS₂ as an electrode material for Mg ion battery: A DFT study, *Appl. Surf. Sci.* **544**, 148775 (2021).
- [18] M. Debbichi, A. Mallah, M. H. Dhaou, and S. Lebègue, First-principles study of monolayer penta-CoS₂ as a promising anode material for Li/Na-ion batteries, *Phys. Rev. Appl.* **16**, 024016 (2021).
- [19] Y. Z. Abdullahi, F. Ersan, E. Akturk, and O. U. Akturk, Theoretical screening of metal borocarbidesheetsfor high-capacity and high-rate Li- and Na-ion batteries, *Phys. Rev. Appl.* **16**, 024031 (2021).
- [20] K.-S. Chen, I. Balla, N. S. Luu, and M. C. Hersam, Emerging opportunities for two-dimensional materials in lithium-ion batteries, *ACS Energy Lett.* **2**, 2026 (2017).
- [21] B. Mendoza-Sanchez and Y. Gogotsi, Synthesis of two-dimensional materials for capacitive energy storage, *Adv. Mater.* **28**, 6104 (2016).
- [22] X. Xu, W. Liu, Y. Kim, and J. Cho, Nanostructured transition metal sulfides for lithium ion batteries: Progress and challenges, *Nano Today* **9**, 604 (2014).
- [23] Z. Du, S. Yang, S. Li, J. Lou, S. Zhang, S. Wang, B. Li, Y. Gong, L. Song, X. Zou, and P. M. Ajayan, Conversion of non-van der Waals solids to 2D transition-metal chalcogenides, *Nature* **577**, 492 (2020).
- [24] J. Shi, Y. Huan, X. Zhao, P. Yang, M. Hong, C. Xie, S. Pennycook, and Y. Zhang, Two-dimensional metallic vanadium ditelluride as a high-performance electrode material, *ACS Nano* **15**, 1858 (2021).
- [25] Z. Huang, X. Han, X. Cui, C. He, J. Zhang, X. Wang, Z. Lin, and Y. Yang, Vertically aligned VS₂ on graphene as a 3D heteroarchitected anode material with capacitance-dominated lithium storage, *J. Mater. Chem. A* **8**, 5882 (2020).
- [26] Y. Zhao, D. Yang, T. He, J. Li, L. Wei, D. Wang, Y. Wang, X. Wang, G. Chen, and Y. Wei, Vacancy engineering in VS₂ nanosheets for ultrafast pseudocapacitive sodium ion storage, *Chem. Eng. J.* **421**, 129715 (2021).
- [27] J. Zhou, L. Wang, M. Yang, J. Wu, F. Chen, W. Huang, N. Han, H. Ye, F. Zhao, Y. Li, and Y. Li, Hierarchical VS₂ nanosheet assemblies: A universal host material for the reversible storage of alkali metal ions, *Adv. Mater.* **29**, 1702061 (2017).
- [28] P. He, M. Yan, G. Zhang, R. Sun, L. Chen, Q. An, and L. Mai, Layered VS₂ nanosheet-based aqueous Zn ion battery cathode, *Adv. Energy Mater.* **7**, 1601920 (2017).
- [29] X. Xue, R. Chen, C. Yan, P. Zhao, Y. Hu, W. Kong, H. Lin, L. Wang, and Z. Jin, One-step synthesis of 2-ethylhexylamine pillared vanadium disulfide nanoflowers with ultralarge interlayer spacing for high-performance magnesium storage, *Adv. Energy Mater.* **9**, 1900145 (2019).
- [30] X. Hu, J. Peng, F. Xu, and M. Ding, Rechargeable Mg²⁺/Li⁺, Mg²⁺/Na⁺, and Mg²⁺/K⁺ hybrid batteries based on layered VS₂, *ACS Appl. Mater. Interfaces* **13**, 57252 (2021).
- [31] W. Li, H. M. Kheimeh Sari, and X. Li, Emerging layered metallic vanadium disulfide for rechargeable metal-ion batteries: Progress and opportunities, *ChemSusChem* **13**, 1172 (2020).
- [32] M. Liu, Z. Zhao, W. Zhang, and W. Zheng, Perspective of vanadium disulfide: A rising star finds plenty of room in single and multielectron energy storage, *Energy Fuels* **36**, 13931 (2022).
- [33] X.-C. Xie, H.-L. Shuai, X. Wu, K.-J. Huang, L.-N. Wang, R.-M. Wang, and Y. Chen, Engineering ultra-enlarged interlayer carbon-containing vanadium disulfide composite for high-performance sodium and potassium ion storage, *J. Alloys Compd.* **847**, 156288 (2020).
- [34] D. Wang, Y. Liu, X. Meng, Y. Wei, Y. Zhao, Q. Pang, and G. Chen, Two-dimensional VS₂ monolayers as potential anode materials for lithium-ion batteries and beyond: First-principles calculations, *J. Mater. Chem. A* **5**, 21370 (2017).
- [35] J. Su, M. Wang, Y. Li, F. Wang, Q. Chen, P. Luo, J. Han, S. Wang, H. Li, and T. Zhai, Sub-millimeter-scale monolayer p-type H-phase VS₂, *Adv. Funct. Mater.* **30**, 2000240 (2020).
- [36] F. Wu, G. T. Kim, M. Kuenzel, H. Zhang, J. Asenbauer, D. Geiger, U. Kaiser, and S. Passerini, Elucidating the effect of iron doping on the electrochemical performance of cobalt-free lithium-rich layered cathode materials, *Adv. Energy Mater.* **9**, 1902445 (2019).
- [37] T.-P. Gao, K. W. Wong, and K. M. Ng, Impacts of morphology and N-doped carbon encapsulation on electrochemical properties of NiSe for lithium storage, *Energy Storage Mater.* **25**, 210 (2020).

- [38] Y. Peng, Y. Bai, C. Liu, S. Cao, Q. Kong, and H. Pang, Applications of metal-organic framework-derived N, P, S doped materials in electrochemical energy conversion and storage, *Coord. Chem. Rev.* **466**, 214602 (2022).
- [39] J. M. Skelton, A. R. Pallipurath, T. H. Lee, and S. R. Elliott, Atomistic origin of the enhanced crystallization speed and n-type conductivity in Bi-doped Ge-Sb-Te phase-change materials, *Adv. Funct. Mater.* **24**, 7291 (2014).
- [40] J. Zhou, G. Zheng, X. Liu, G. Dong, and J. Qiu, Defect engineering in lanthanide doped luminescent materials, *Coord. Chem. Rev.* **448**, 214178 (2021).
- [41] G. Clavel, M. G. Willinger, D. Zitoun, and N. Pinna, Solvent dependent shape and magnetic properties of doped ZnO nanostructures, *Adv. Funct. Mater.* **17**, 3159 (2007).
- [42] Y. Wang, V. Yannello, J. Graterol, H. Zhang, Y. Long, and M. Shatruk, Theoretical and experimental insights into the effects of Zn doping on the magnetic and magnetocaloric properties of MnCoGe, *Chem. Mater.* **32**, 6721 (2020).
- [43] H. Zhang, X. Liu, J. Wang, B. Zhang, J. Chen, L. Yang, G. Wang, M. Li, Y. Zheng, X. Zhou, and G. Han, Solution-synthesized SnSe_{1-x}S_x: Dual-functional materials with enhanced electrochemical storage and thermoelectric performance, *ACS Appl. Mater. Interfaces* **13**, 37201 (2021).
- [44] N. Shi, B. Xi, M. Huang, F. Tian, W. Chen, H. Li, J. Feng, and S. Xiong, One-step construction of MoS_{0.74}Se_{1.26}/N-doped carbon flower-like hierarchical microspheres with enhanced sodium storage, *ACS Appl. Mater. Interfaces* **11**, 44342 (2019).
- [45] Q. Gou, J. Xu, H. Luo, J. Wang, B. Zhang, J. Deng, N. A. N. Ouedraogo, Y. Zheng, S. Lu, J. Xiao, K. Sun, and M. Li, Heteroatom doping strategy enables bi-functional electrode with superior electrochemical performance, *Electrochim. Acta* **431**, 141127 (2022).
- [46] J. Jian, H. Chang, P. Dong, Z. Bai, and K. Zuo, A mechanism for the variation in the photoelectric performance of a photodetector based on CVD-grown 2D MoS₂, *RSC Adv.* **11**, 5204 (2021).
- [47] J. Shi, B. Jiang, C. Li, Z. Liu, F. Yan, X. Liu, H. Li, C. Yang, D. Dong, and J. Hao, Study on capacitance properties of the sputtered carbon doped titanium nitride electrode material for supercapacitor, *Vacuum* **198**, 110893 (2022).
- [48] S. Tomar, P. Sen, and S. Chakraborty, Single atom functionalization in vanadium dichalcogenide monolayers: Towards enhanced electrocatalytic activity, *Sustainable Energy Fuels* **6**, 5337 (2022).
- [49] J. Woo, E. S. Sim, M. Je, H. Choi, and Y.-C. Chung, Theoretical dopant screening and processing optimization for vanadium disulfide as cathode material for Li-air batteries: A density functional theory study, *Appl. Surf. Sci.* **508**, 145276 (2020).
- [50] Q. Tang, Z. Zhou, and P. Shen, Are MXenes promising anode materials for Li ion batteries? Computational studies on electronic properties and Li storage capability of Ti₃C₂ and Ti₃C₂X₂ (X = F, OH) monolayer, *J. Am. Chem. Soc.* **134**, 16909 (2012).
- [51] G. Wang, Z. Ma, J.-W. Jiang, J.-k. Yang, Y.-L. Sun, Z.-F. Qian, P. Huang, P. Zhang, and S.-H. Wei, Crystal structures and physicochemical properties of Be₂N and Mg₂N as electride materials, *Phys. Rev. Appl.* **19**, 034014 (2023).
- [52] A. Omidvar, Assessment of boroxine covalent organic framework as Li-ion battery anodes, *J. Mol. Liq.* **339**, 116822 (2021).
- [53] X. Zhang, Z. Yu, S.-S. Wang, S. Guan, H. Y. Yang, Y. Yao, and S. A. Yang, Theoretical prediction of MoN₂ monolayer as a high capacity electrode material for metal ion batteries, *J. Mater. Chem. A* **4**, 15224 (2016).
- [54] S. Nosé, A molecular dynamics method for simulations in the canonical ensemble, *Mol. Phys.* **52**, 255 (1984).
- [55] D. B. Putungan, S. H. Lin, and J. L. Kuo, Metallic VS₂ monolayer polytypes as potential sodium-ion battery anode via ab initio random structure searching, *ACS Appl. Mater. Interfaces* **8**, 18754 (2016).
- [56] H. Zhang, L.-M. Liu, and W.-M. Lau, Dimension-dependent phase transition and magnetic properties of VS₂, *J. Mater. Chem. A* **1**, 10821 (2013).
- [57] See Supplemental Material at <http://link.aps.org/supplemental/10.1103/PhysRevApplied.21.024038> for additional information, such as the structural parameters of VS_xO_yC_z monolayers with and without Mg adsorption.
- [58] See Supplemental Material at <http://link.aps.org/supplemental/10.1103/PhysRevApplied.21.024038> for additional information, such as the radius of the sulfur atom.
- [59] See Supplemental Material at <http://link.aps.org/supplemental/10.1103/PhysRevApplied.21.024038> for additional information, such as the radius of the oxygen atom.
- [60] Y. Kong, H. Ai, W. Wang, X. Xie, K. H. Lo, S. Wang, and H. Pan, Waved 2D transition-metal disulfides for nanodevices and catalysis: A first-principle study, *ACS Appl. Nano Mater.* **3**, 2804 (2020).
- [61] C. Tantardini and A. R. Oganov, Thermochemical electronegativities of the elements, *Nat. Commun.* **12**, 2087 (2021).
- [62] J. Lin, T. Yu, F. Han, and G. Yang, Computational predictions of two-dimensional anode materials of metal-ion batteries, *WIREs Comput. Mol. Sci.* **10**, e1473 (2020).
- [63] T. Yu, Z. Zhao, L. Liu, S. Zhang, H. Xu, and G. Yang, TiC₃ Monolayer with high specific capacity for sodium-ion batteries, *J. Am. Chem. Soc.* **140**, 5962 (2018).
- [64] See Supplemental Material at <http://link.aps.org/supplemental/10.1103/PhysRevApplied.21.024038> for additional information about the role of Zr doping in stabilizing Li[Ni_{0.6}Co_{0.2}Mn_{0.2}]O₂ as a cathode material for lithium-ion batteries and the increment diffusion energy of Li.
- [65] See Supplemental Material at <http://link.aps.org/supplemental/10.1103/PhysRevApplied.21.024038> for additional information about boron-doped sodium-layered oxides for sodium-ion battery cathodes and the increment diffusion energy of Na.
- [66] See Supplemental Material at <http://link.aps.org/supplemental/10.1103/PhysRevApplied.21.024038> for additional information, such as diffusion energies with increasing B by doping Al in Ni-rich layered oxide cathode materials.
- [67] See Supplemental Material at <http://link.aps.org/supplemental/10.1103/PhysRevApplied.21.024038> for additional information, such as the increase in diffusion energy of Li after W doping on Ni-rich NCM (LiNi_xCo_yMn_zO₂) cathodes.
- [68] See Supplemental Material at <http://link.aps.org/supplemental/10.1103/PhysRevApplied.21.024038> for additional

- information, such as the increase in diffusion energy of Na after Se doping.
- [69] See Supplemental Material at <http://link.aps.org/supplemental/10.1103/PhysRevApplied.21.024038> for additional information, such as the increase in diffusion energy of Zn after S-doped MnOOH nanofiber.
- [70] See Supplemental Material at <http://link.aps.org/supplemental/10.1103/PhysRevApplied.21.024038> for additional information, such as the increase in diffusion energy of Li after Tb-doped TiNb₂O₇.
- [71] See Supplemental Material at <http://link.aps.org/supplemental/10.1103/PhysRevApplied.21.024038> for additional information, such as the increase in diffusion energy of Na after Ni-doped *P2*-type layered oxide cathodes can effectively promote deintercalation and intercalation of Na.